Development of Numerical Program on 2-Dimensional Inviscid Burgers Equation in Finite Volume Method with UPWIND and TVD Scheme

Roby Pratama Sitepu[1], Timotius Dimas Narendra B.[1] & Muhammad Arviano Yuono[2]

[1]Mechanical Engineering Master Study Program, Faculty of Mechanical and Aerospace Engineering, Institut Teknologi Bandung, Jl Ganesha 10, Bandung, 40132, Indonesia
[2]Aerospace Engineering Master Study Program, Faculty of Mechanical and Aerospace Engineering, Institut Teknologi Bandung, Jl Ganesha 10, Bandung, 40132, Indonesia
Email: 23125060@mahasiswa.itb.ac.id

Abstract. This paper presents the development and validation of a numerical solver for the two-dimensional steady-state inviscid Burgers equation using the Finite Volume Method (FVM). The Burgers equation serves as a fundamental model for studying nonlinear wave propagation and shock formation in hyperbolic conservation laws. Two numerical schemes are implemented and compared: the first-order Upwind scheme and high-resolution Total Variation Diminishing (TVD) schemes with various flux limiters including Min-Mod, Van Leer, Superbee, QUICK, and UMIST. The numerical solutions are validated against an exact analytical solution derived using the method of characteristics. Results demonstrate that while the Upwind scheme is robust and stable, it exhibits significant numerical diffusion that smears shock discontinuities. In contrast, TVD schemes achieve sharper shock resolution while maintaining monotonicity. The upwind scheme spreads the shock over 3.86 cells, whereas the limiters confine it to between 1.73 and 1.91 cells, reduce the L1 error by 60 to 67 per cent and reproduce the total variation of the exact solution exactly. Superbee gives the sharpest shock and QUICK the lowest L2 error, while Min-Mod is the most diffusive of the limiters; the most compressive limiters, however, only reach a steady state once the CFL number is reduced. A refinement study over nine grids gives observed orders of accuracy of 0.86 in L1 and 0.52 in L2 with a non-convergent maximum error, which is the behaviour expected of a first-order monotone scheme applied to a discontinuous solution.

Keywords: *burgers equation, finite volume method, flux limiters, TVD, upwind scheme, shock capturing.*

1 Introduction

The Inviscid Burgers equation stands as a cornerstone in the field of computational fluid dynamics (CFD) and applied mathematics, representing one of the simplest forms of a non-linear hyperbolic conservation law [1]. Initially

Received April 9th, 2026, July 20th, 2026, Accepted for publication August 13th 2026
Copyright ©2026 Published by Faculty of Mechanical and Aerospace Engineering ITB
ISSN: 0852-6095, DOI: 10.5614/MESIN.2026.31.1.3.

proposed by Johannes Martinus Burgers in 1948 as a model for turbulence, it has since found extensive applications ranging from gas dynamics and acoustic waves to the modeling of traffic flow density [2], [3]. Its primary significance lies in its structural similarity to the full Navier-Stokes equations; by retaining the convective non-linearity while discarding the viscous diffusion term, it isolates the mathematical mechanism responsible for the steepening of waves and the eventual formation of shocks [1]. Consequently, studying this equation provides a controlled environment for understanding the complex behaviors of non-linear waves, making it an indispensable first step for researchers aiming to master the intricacies of compressible flow simulations [1].

Developing a robust numerical solver for the Burgers equation, particularly using the Finite Volume Method (FVM), is motivated by the necessity to accurately capture discontinuous solutions that are characteristic of hyperbolic systems [4]. Unlike Finite Difference Methods (FDM) which often rely on the differential form of governing equations and may struggle with discontinuities, the FVM is based on the integral form of conservation laws [4]. This distinction is critical because it ensures that quantities such as mass, momentum, and energy are strictly conserved across control volumes, a property that must be maintained to correctly predict the propagation speed of shock waves in accordance with the Rankine-Hugoniot conditions [4], [5]. Furthermore, the development of an in-house FVM code offers a granular level of control over the discretization process, allowing for a deep exploration of how numerical fluxes are approximated at cell interfaces [4]. Building the solver in-house also keeps every step of the flux discretisation explicit, which is a prerequisite for the verification exercise reported here: each scheme can be exercised on identical grids, with identical boundary treatment and convergence criteria, and compared against a closed-form solution, without the confounding influence of the proprietary limiters and implicit stabilisation used in general-purpose CFD packages [6].

However, the numerical treatment of non-linear convection poses significant challenges, necessitating the study and comparison of different solver types. It is a well-known consequence of Godunov's order barrier theorem that linear numerical schemes cannot simultaneously be high-order accurate and monotonicity-preserving [7]. Simple first-order schemes, such as the standard Upwind method, are unconditionally stable and monotonic but suffer from excessive numerical diffusion, which manifests as the artificial smearing of sharp shock fronts [4]. Conversely, traditional high-order schemes tend to introduce spurious oscillations, known as the Gibbs phenomenon, in the vicinity of discontinuities, which can destabilize the solution and lead to unphysical results [8].

To bridge the gap between stability and accuracy, it becomes essential to investigate high-resolution schemes, specifically those utilizing the Total Variation Diminishing (TVD) property [8]. These modern solvers employ non-linear flux limiters, such as Min-Mod, Superbee, and Van Leer, to adaptively control the numerical flux [9]. By acting as a high-order scheme in smooth regions of the flow and reverting to a first-order scheme near shocks, TVD methods attempt to resolve discontinuities with high precision without introducing numerical oscillations [8], [9]. A comparative study of these different limiters is vital because no single limiter preserves all features of a flow field perfectly; some may be too compressive, turning smooth waves into shocks (squaring effect), while others may remain too diffusive [9]. A quantitative comparison of limiters on a problem whose exact solution is known is therefore useful, because it isolates the effect of the limiter from every other modelling choice.

The scope of the present work is deliberately narrow. This paper does not propose a new scheme, nor does it attempt a comprehensive survey of shock-capturing methods. It reports the implementation and verification of a finite volume solver for a two-dimensional steady inviscid Burgers problem for which an exact solution is available in closed form, and uses that solution to quantify the behaviour of the first-order upwind scheme and of six standard TVD limiters in terms of observed order of accuracy, shock thickness, total variation and computational cost.

In this study, the focus is on the two-dimensional steady-state inviscid Burgers equation to perform such a comparative analysis. By implementing and benchmarking the classical Upwind scheme against a suite of TVD schemes with differing flux limiters, we aim to quantify their performance in terms of shock resolution capability, error magnitude, and computational cost.

2 Methodology

2.1 Governing Equation

The 2D inviscid Burgers equation in conservative form is:

$$\frac{\partial u}{\partial t} + \frac{\partial E}{\partial x} + \frac{\partial F}{\partial y} = 0 \tag{1}$$

Where the flux functions are defined as:

Nonlinear flux in x-direction:

$$E(u) = \frac{au^2}{2} \tag{2}$$

Linear flux in y-direction:

$$F(u) = bu \tag{3}$$

In vector notation:

$$\frac{\partial u}{\partial t} + \nabla \cdot \vec{H} = 0 \tag{4}$$

Where

$$\vec{H} = (E, F) \tag{5}$$

Is the flux vector.
In these expressions u(x, y) is the transported scalar, t is the pseudo-time used to march the solution to steady state, and x and y are the Cartesian coordinates of the unit square. E(u) and F(u) denote the flux components in the x- and y-directions respectively, H = (E, F) is the flux vector, a is the coefficient of the nonlinear convection term and b the coefficient of the linear advection term. All quantities are dimensionless.

The flux pair adopted here is nonlinear in x and linear in y, which differs from the classical two-dimensional Burgers equation in which the convection is nonlinear in both directions. The reason for this choice is that it makes the steady problem exactly solvable while preserving the mechanism the solver is meant to reproduce. Setting the time derivative to zero and dividing by b, the governing equation reduces to

$$\partial u/\partial y + (a/b)\cdot u\cdot \partial u/\partial x = 0$$

which is formally identical to the one-dimensional unsteady inviscid Burgers equation, with the vertical coordinate y acting as a time-like variable and a/b as a scaled wave speed. The linear flux in y fixes a single unambiguous marching direction, so the steady two-dimensional boundary value problem inherits the whole classical theory of the one-dimensional initial value problem: the characteristics are straight lines, the location at which the solution first becomes multivalued follows from the focusing of those characteristics, and the solution beyond that point is fixed by the Rankine–Hugoniot condition [4], [5], [15]. The configuration is therefore a benchmark with an exact reference solution against which a shock-capturing implementation can be verified, which is not generally

available for the doubly nonlinear form. A further consequence, used in Section 4.4, is that the steady solution depends on a and b only through the ratio a/b.

2.2 Problem Domain and Boundary Conditions

The computational domain is the unit square $\Omega = [0,1] \times [0,1]$. The domain is discretized using a uniform structured grid with $N \times N$ points.

The problem parameters are characterized by:

- a: Nonlinear convection coefficient in x-direction
- b: Linear advection coefficient in y-direction
- c: Left boundary value
- d: Right boundary value

For the reference case (Case 1): $a = 1.0, b = 1.0, c = 1.5, d = -0.5$.

Boundary Conditions:

- Left Boundary ($x = 0$): Dirichlet condition $u(0, y) = c = 1.5$
- Right Boundary ($x = 1$): Dirichlet condition $u(1, y) = d = -0.5$
- Bottom Boundary ($y = 0$): Linear function $u(x, 0) = 1.5 - 2x$
- Top Boundary ($y = 1$): Neumann outflow condition $\frac{\partial u}{\partial y}|_{y=1} = 0$

2.3 Finite Volume Method Discretization

The Finite Volume Method (FVM) directly approximates the integral form of conservation laws [4]. Starting from the differential conservation law and applying the Gauss divergence theorem [1]:

$$\frac{\partial}{\partial \mathrm{t}} \int_{\mathrm{V_c}} \mathrm{u}\ \mathrm{dV} + \oint_{\partial \mathrm{V_c}} \vec{\mathrm{H}} \cdot \vec{\mathrm{n}}\, \mathrm{dS} = 0 \tag{6}$$

For a rectangular cell (i, j) with dimension $\Delta x \times \Delta y$, the semi-discrete equation becomes:

$$\frac{du_{i,j}}{dt} = -\frac{a}{2\Delta x}(\phi_e^2 - \phi_w^2) - \frac{b}{\Delta y}(\phi_n - \phi_s) \tag{7}$$

The face flux contributions are:

Here the subscripts e, w, n and s denote the east, west, north and south faces of the control volume centred on node (i, j); φ is the value of u reconstructed at a face, Δx and Δy are the uniform grid spacings, and N is the number of nodes in each direction, so that Δx = Δy = 1/(N − 1). The subscripts C, E, W, N and S refer to the centre, east, west, north and south neighbouring nodes.text

- East Face: $\text{Flux}_e = \frac{a}{2}\phi_e^2 \cdot \Delta y$
- West Face: $\text{Flux}_w = \frac{a}{2}\phi_w^2 \cdot \Delta y$
- North Face: $\text{Flux}_n = b\phi_n \cdot \Delta x$
- South Face: $\text{Flux}_s = b\phi_s \cdot \Delta x$

2.4 Upwind Scheme

The upwind scheme determines face values based on the direction of wave propagation, providing stability for convection-dominated problems [4], [5].

2.4.1 X-Direction (Nonlinear Flux)

For wave speed $\lambda_e = a \cdot \frac{u_C + u_E}{2}$:

- If $\lambda_e \geq 0$: $\phi_e = u_C$ (upwind from center)
- If $\lambda_e < 0$: $\phi_e = u_E$ (upwind from east neighbor)

λ_e is the wave speed evaluated at the east face; because the x-flux is nonlinear this speed depends on the solution itself, whereas in the y-direction the wave speed is the constant b.text

2.4.2 Y-Direction (Linear Flux)

For wave speed $\lambda_y = b$:

- If $b \geq 0$: $\phi_n = u_C, \phi_s = u_S$
- If $b < 0$: $\phi_n = u_N, \phi_s = u_C$

2.4.3 Numerical Diffusion:

The first-order upwind scheme has inherent numerical diffusion of order $O(\Delta x)$ [4]. This diffusion smears discontinuities but ensures stability and monotonicity with no spurious oscillations near shocks.

2.5 Total Variation Diminishing (TVD) Schemes

TVD schemes achieve higher-order accuracy while preventing spurious oscillations near discontinuities [8]. The total variation of a numerical solution is:

$$TV(u^n) = \sum_j \left| u_{j+1}^n - u_j^n \right| \tag{8}$$

A scheme is TVD if: $TV(u^{n+1}) \leq TV(u^n)$.

2.5.1 TVD Face Value Reconstruction

$$\phi_f = \phi_U + \frac{1}{2}\psi(r)(\phi_D - \phi_U) \tag{9}$$

where:

- ϕ_U: Upwind cell value
- ϕ_D: Downwind cell value
- $\psi(r)$: Flux limiter function
- r: Gradient ratio

2.5.2 Gradient Ratio Computation

For the east face $(i + \frac{1}{2})$:

Positive flow $(\lambda_x \geq 0)$:

$$r_e = \frac{u_{i,j} - u_{i-1,j}}{u_{i+1,j} - u_{i,j} + \epsilon} \tag{10}$$

Negative flow $(\lambda_x < 0)$:

$$r_e = \frac{u_{i+1,j} - u_{i+2,j}}{u_{i,j} - u_{i+1,j} + \epsilon} \tag{11}$$

A small parameter $\epsilon \approx 10^{-10}$ prevents division by zero [9].

In the reconstruction, φ_U and φ_D are the values at the upwind and downwind nodes of the face being evaluated, r is the ratio of the upwind to the downwind solution gradient, ψ(r) is the flux limiter and ε is the regularisation constant introduced above. TV denotes the total variation of the discrete solution.text

2.5.3 Flux Limiter Functions:

1. Min-Mod Limiter [9]:

$$\psi(r) = \max(0, \min(1, r)) \tag{12}$$

2. Van Leer Limiter [10]:

$$\psi(r) = \frac{r+|r|}{1+|r|} \tag{13}$$

3. Albada Limiter [11]:

$$\psi(r) = \frac{r^2+r}{r^2+1} \tag{14}$$

4. Superbee Limiter [9]:

$$\psi(r) = \max(0, \min(1,2r), \min(2, r)) \tag{15}$$

5. QUICK Limiter [12]:

$$\psi(r) = \max\left(0, \min\left(2,2r, \frac{3+r}{4}\right)\right) \tag{16}$$

6. UMIST Limiter [13]:

$$\psi(r) = \max\left(0, \min\left(2r, \frac{1+3r}{4}, \frac{3+r}{4}, 2\right)\right) \tag{17}$$

2.6 Explicit Time Stepping

The solution is advanced in time using and explicit Euler method [1]:

$$u_{i,j}^{n+1} = u_{i,j}^{n} - \Delta t \left[\frac{E_{i+1/2}-E_{i-1/2}}{\Delta x} + \frac{F_{j+1/2}-F_{j-1/2}}{\Delta y}\right]^n \tag{18}$$

The time step Δt is constrained by the CFL condition for stability [14]. The time loop continues until steady state is reached ($residual < 10^{-6}$).

2.7 Cases and Evaluation Method

This study evaluates the numerical solver using multiple test cases and a structured comparison workflow. The methodology includes case definition, solver execution, and quantitative comparison against the analytical solution.

2.7.1 Case Definitions

The following cases area considered to study the effect of convection and boundary parameters:

Table 1 Cases definition for each case

Case	a	b	c (left)	d (right)	Notes
Case 1	1.0	1.0	1.5	-0.5	Reference case; used for grid convergence and solver comparison
Case 2	1.0	0.5	1.5	-0.5	Reduced vertical advection
Case 3	2.0	1.0	1.5	-0.5	Increased nonlinear convection
Case 4	1.0	1.0	1.0	-0.6	Weak shock case

2.7.2 Solver Comparison (Case 1)

For Case 1, multiple solvers are compared to quantify accuracy and shock resolution:

1. First-order upwind scheme (baseline)
2. TVD schemes with flux limiters: Min-Mod, Van Leer, Albada, Superbee, QUICK, and UMIST

All solvers are evaluated on the same grid size ($N = 41$ for limiter comparison) and compared against the analytical solution using L1, L2, and L-infinity error norms, as well as qualitative contour and surface comparisons.

2.7.3 Comparisons Between Cases

After validating against Case 1, the solver is applied to Cases 2-4. The comparison focuses on:

1. Changes in shock angle predicted by the ratio of characteristic speeds
2. Differences in shock location and rarefaction spread
3. Convergence behavior and stability for each parameter set

This case study provides a comprehensive evaluation of solver robustness and sensitivity to physical parameters.

3 Analytical Benchmark Solution

3.1 Exact Solution Used for Verification

The exact solution of the steady problem is used in this work solely as a benchmark against which the numerical solver is verified; it is not itself a new result. It is obtained by the method of characteristics, and because the steady equation is equivalent to a one-dimensional initial value problem in the time-like coordinate y, the construction is valid for arbitrary a, b, c and d. An exact solution is therefore available for every case in Table 1, and the resulting shock parameters for all four cases are collected in Table 5. The full derivation, together with the explicit piecewise solution for the reference case (Case 1), is given in the Appendix.

Case 1 is used for the quantitative verification in Section 4 because it is the only one of the four configurations in which the shock remains inside the computational domain over the full height of the domain while the imposed boundary conditions stay compatible with the characteristics. In Cases 2 and 3 the shock reaches the right boundary at y = 0.5, beyond which the Dirichlet condition u(1, y) = d is no longer consistent with the outgoing characteristics and that boundary in effect becomes an outflow; the exact and discrete problems then differ in a boundary layer one cell wide. Case 4 has a weaker jump and its shock forms higher in the domain, at y = 0.625. The exact solutions for Cases 2 to 4 are nevertheless reported in the Appendix and are used for the error norms quoted in Section 4.4.

3.2 Boundary Conditions Derivations and Conclusions

The boundary conditions are a critical component of the problem definition. For Case 1, they are derived as follows:

1. Left Boundary ($x = 0$): The problem specifies a Dirichlet condition $u(0, y) = c$. For Case 1, $c = 1.5$. Thus:

   $$u(0, y) = 1.5 \tag{19}$$

2. Right Boundary ($x = 1$): Similarly, defined by $u(1, y) = d$. For case 1, $d = -0.5$. Thus:

   $$u(1, y) = -0.5 \tag{20}$$

3. Bottom Boundary ($y = 0$): The condition is a linear interpolation between the left and right values at $y = 0$:

$$u(x, 0) = c + \frac{d-c}{1-0}(x - 0) \quad (21)$$

Substituting $c = 1.5$ and $d = -0.5$:

$$u(x, 0) = 1.5 + (-0.5 - 1.5)x = 1.5 - 2x \quad (22)$$

This linear profile is the source of the compression wave.

4. Top Boundary ($y = 1$): A Neumann outflow condition is applied, assuming the flow leaves the domain without change:

$$\frac{\partial u}{\partial y}|_{y=1} = 0 \quad (23)$$

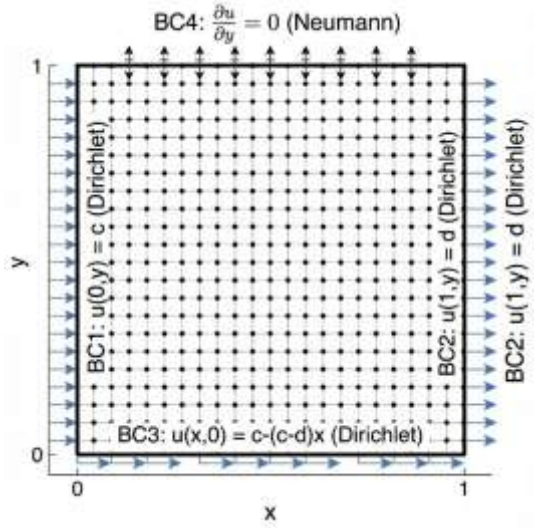


Figure 1 Computational domain and boundary conditions

Substituting the derived analytical solution back into the boundary conditions confirm its validity:

- At $x = 0$ (in Region 1): $u(0, y) = 1.5$ (matches)
- At $x = 1$ (in Region 3): $u(1, y) = -0.5$ (matches)
- At $y = 0$: $\frac{1.5-2x}{1-2(0)} = 1.5 - 2x$ (matches)

Thus, the piecewise analytical solution is consistent with all physical boundary conditions derived for this problem.

4 Results and Discussion

4.1 Simulation Parameters

The numerical simulations were performed with the following parameters:

- CFL number: 0.5
- Convergence tolerance: 10^{-6}
- Problem parameters as shown in the case table (Section 2)

For Case 1, grid convergence test was conducted using:

$$\mathrm{N} = [21,26,31,\ldots,196,201] \tag{24}$$

The L2 error was computed against the analytical solution to determine a suitable grid resolution.

4.2 Upwind Scheme Results

4.2.1 Grid Convergence Test

The grid convergence test results are shown in Figure 2. The L2 error decreases monotonically with increasing grid density, confirming the consistency of the numerical method. Based on the convergence and computational cost trade-off, $\mathrm{N} = 201$ is selected as the reference high-resolution grid.

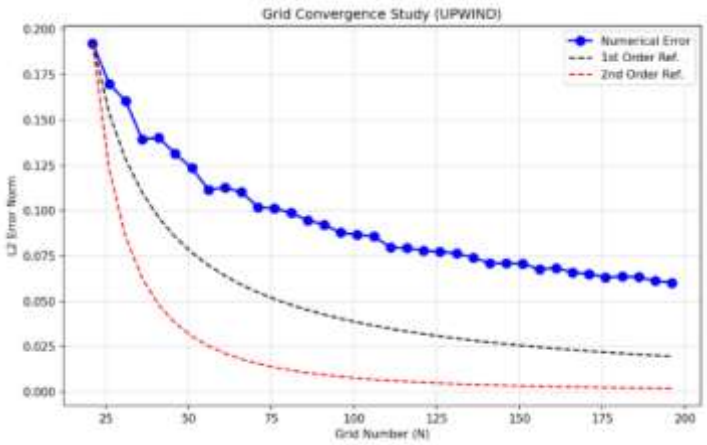


Figure 2 Plot of the L2 error versus number of simulation grid points

4.2.2 2 Dimension Contour Comparisons

The 2D contour plots compare the spatial distribution of the numerical solution (left) against the analytical solution (right). Across $N = 21, N = 41$, and $N = 201$, the main differences appear near the shock line: coarse grids show a wider smeared region, while higher resolution sharpens the discontinuity and better matches the analytical profile.

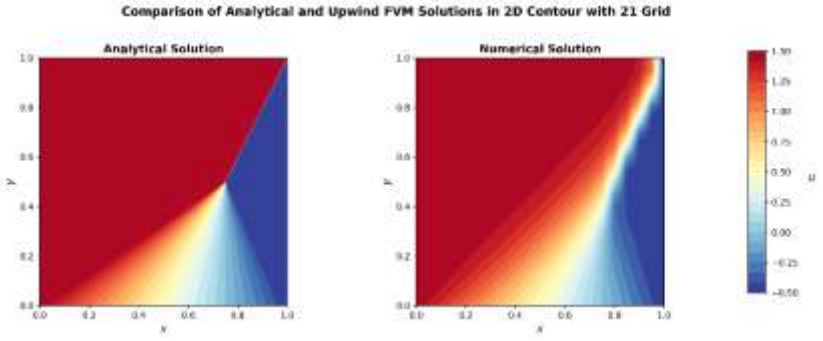


Figure 3 2D contour comparison – analytical solution (left) vs Upwind scheme (right) for N = 21

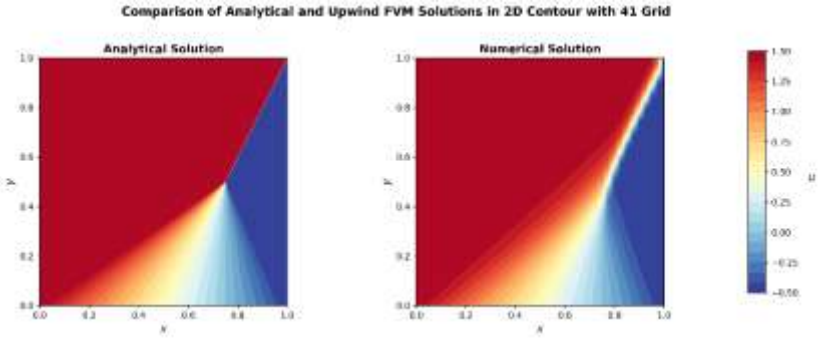


Figure 4 2D contour comparison – analytical solution (left) vs Upwind scheme (right) for N = 41

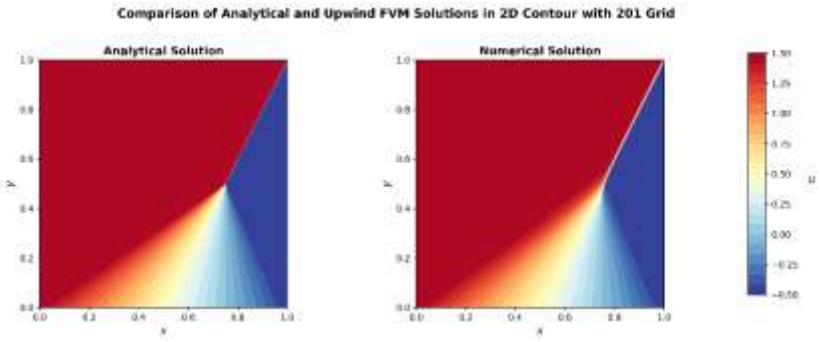


Figure 5 2D contour comparison – analytical solution (left) vs Upwind scheme (right) for N = 201

4.2.3 3 Dimension Surface Comparisons

The 3D surface plots provide a clearer view of shock steepness and overall solution topology. The three grids ($N = 21, N = 41, N = 201$) highlight how the upwind scheme smooths the discontinuity at coarse resolution and gradually recovers the sharp transition as the grid is refined. These figures emphasize the diffusion-dominated nature of first-order upwind while confirming convergence toward the analytical surface.

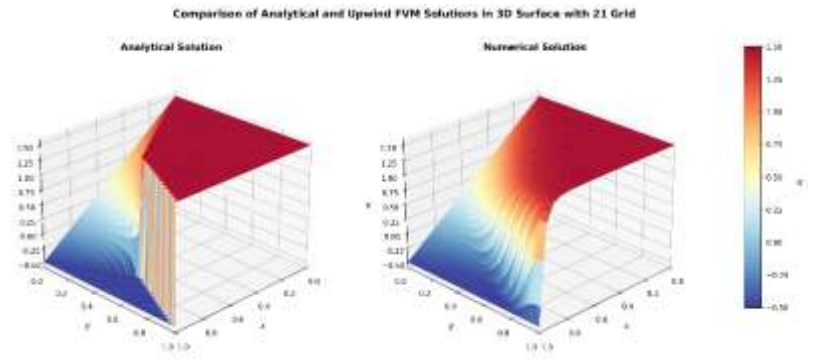


Figure 6 3D surface comparison – analytical solution (left) vs Upwind scheme (right) for N = 21

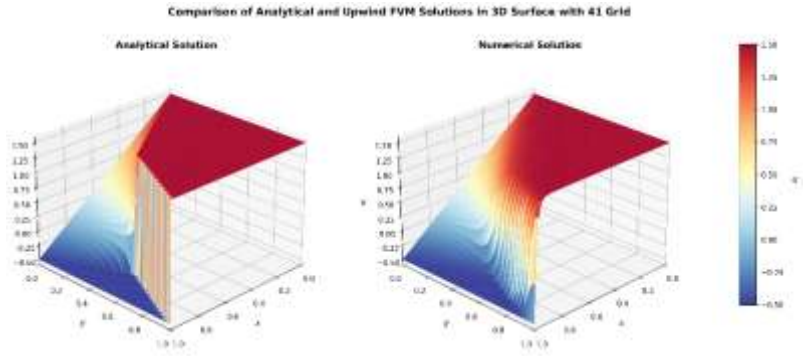


Figure 7 3D surface comparison – analytical solution (left) vs Upwind scheme (right) for N = 41

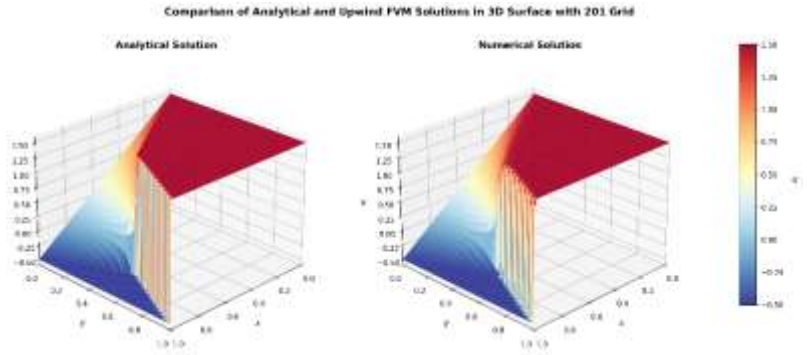


Figure 8 3D surface comparison – analytical solution (left) vs Upwind scheme (right) for N = 201

4.2.4 Error Analysis

The error metrics in Table 2 quantify how grid refinement improves agreement with the analytical solution. As the grid is refined from $N = 21$ to $N = 201$, L1 and L2 errors decrease consistently, indicating convergence of the numerical method. The relative L2 error shows the same trend, confirming that the solution accuracy improves with resolution and that the upwind scheme is consistent for this problem.

The table also reports iteration counts and residual levels, which demonstrate that all cases reached the same convergence tolerance. The largest discrepancies are concentrated near the shock, so even when global errors decrease, the L-infinity metric remains high because it captures the peak local error at the discontinuity.

Table 2 Error metrics for different grid size

Metric	N = 21	N = 41	N = 201
Converged	Yes	Yes	Yes
Iterations	104	179	715
Final Residual	$9.87\ 10^{-7}$	$9.66\ 10^{-7}$	$9.46\ 10^{-7}$
Time Elapsed (s)	0.007	0.020	0.801
L_1 Error	0.0700	0.0412	0.0102
L_2 Error	0.1924	0.1403	0.0602
L_∞ Error	1.4073	1.4777	1.6087
Relative L_2	0.1547	0.1122	0.0479

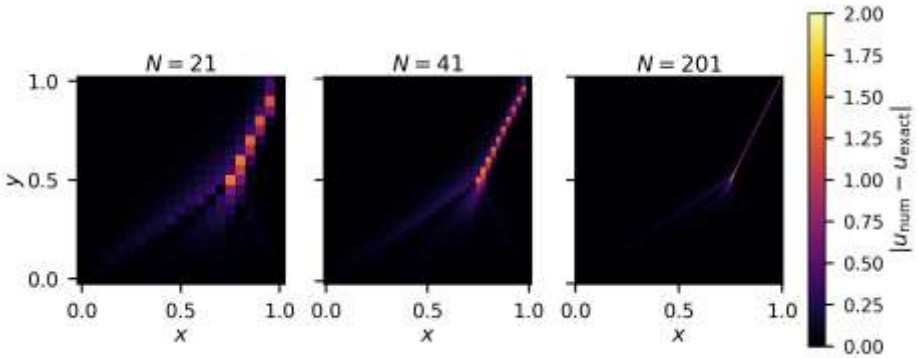


Figure 9 Error field for $N = 21, 41$ and 201 (upwind vs analytical)

Observation:

1. Shock Capturing: The upwind scheme captures the shock formation, but at lower grid quality ($N = 21$ and $N = 41$) the discontinuity is visibly smeared due to numerical diffusion. This reinforces the need for higher grid resolution when using a first-order scheme.
2. Stability: For all grid sizes, the scheme remains stable and monotone, with no spurious oscillations near the shock.

3. Discontinuity: Even at $N = 201$, the shock remains thicker than the analytical solution because of the first-order nature of upwinding. The error field indicates that the largest discrepancies concentrate along the discontinuity at $y > 0.5$.

4.2.5 Observed Order of Accuracy

Table 2 shows that the error falls as the mesh is refined, but it does not by itself establish the rate at which it does so. The upwind scheme was therefore run on nine grids between N = 21 and N = 401, and the observed order of accuracy p was extracted from a least-squares fit of log(error) against log h, with h = 1/(N − 1). The error norms are listed in Table 3 and the fit is shown in Figure 10.

Table 3 Grid refinement study and observed order of accuracy for the first-order upwind scheme (Case 1).

N	h	L1 error	L2 error	L∞ error	Iterations
21	0.05000	0.07001	0.19242	1.4073	104
41	0.02500	0.04117	0.14032	1.4777	179
61	0.01667	0.02919	0.11288	1.5137	250
81	0.01250	0.02296	0.09883	1.5375	319
101	0.01000	0.01881	0.08694	1.5554	386
141	0.00714	0.01387	0.07109	1.5767	519
201	0.00500	0.01018	0.06020	1.6087	715
281	0.00357	0.00747	0.04921	1.6326	972
401	0.00250	0.00543	0.04125	1.6582	1353

The fitted rates are p(L1) = 0.86, p(L2) = 0.52 and p(L∞) = -0.05. Only the L1 rate approaches the first-order behaviour expected of the upwind scheme, and the discontinuity is the reason. A first-order monotone scheme spreads a shock over a fixed number of cells, so the pointwise error in that layer stays of the order of the jump however fine the mesh becomes: the error is O(1) on a strip whose width shrinks in proportion to h. Integrating over that strip gives an L1 error of O(h) and an L2 error of O(√h), while the maximum error does not fall at all. The measured values follow this prediction closely, 0.86 against 1 in L1 and 0.52 against 0.5 in L2, and the L_∞ norm is essentially flat. It in fact drifts slightly upwards, from 1.4073 at N = 21 to 1.6582 at N = 401, because on finer grids a sampling point falls ever closer to the exact discontinuity. The formal first-order accuracy of the implementation is therefore confirmed in the only norm in which first order is attainable for a discontinuous solution, and the apparently anomalous

growth of L_∞ already visible in Table 2 is a property of the exact solution rather than a defect of the solver [4], [18], [19].

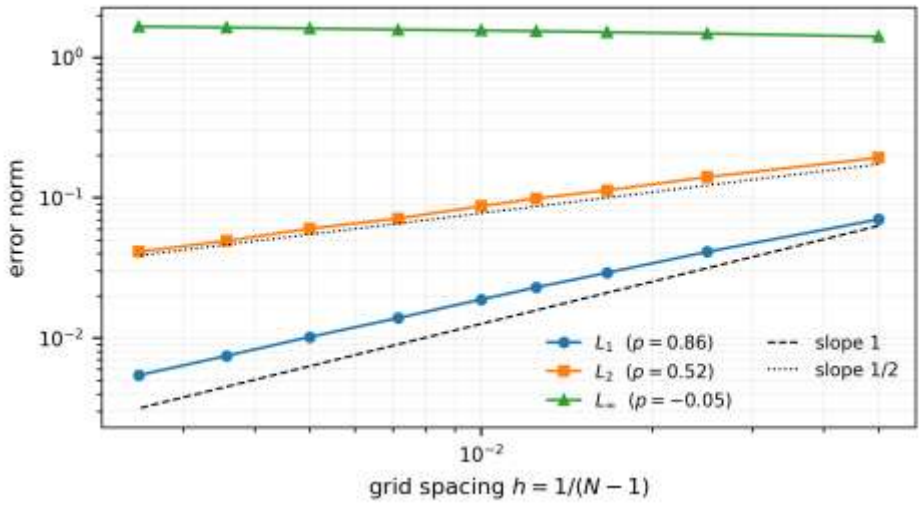


Figure 10 Convergence of the L1, L2 and L∞ error norms of the upwind scheme under grid refinement, with the fitted observed orders.

4.3 TVD Scheme Results

The TVD results are evaluated at $N = 41$ to balance accuracy and computational cost. All limiters reduce numerical diffusion relative to the first-order upwind scheme by applying nonlinear reconstruction only in smooth regions, while reverting to first order near shocks to preserve monotonicity.

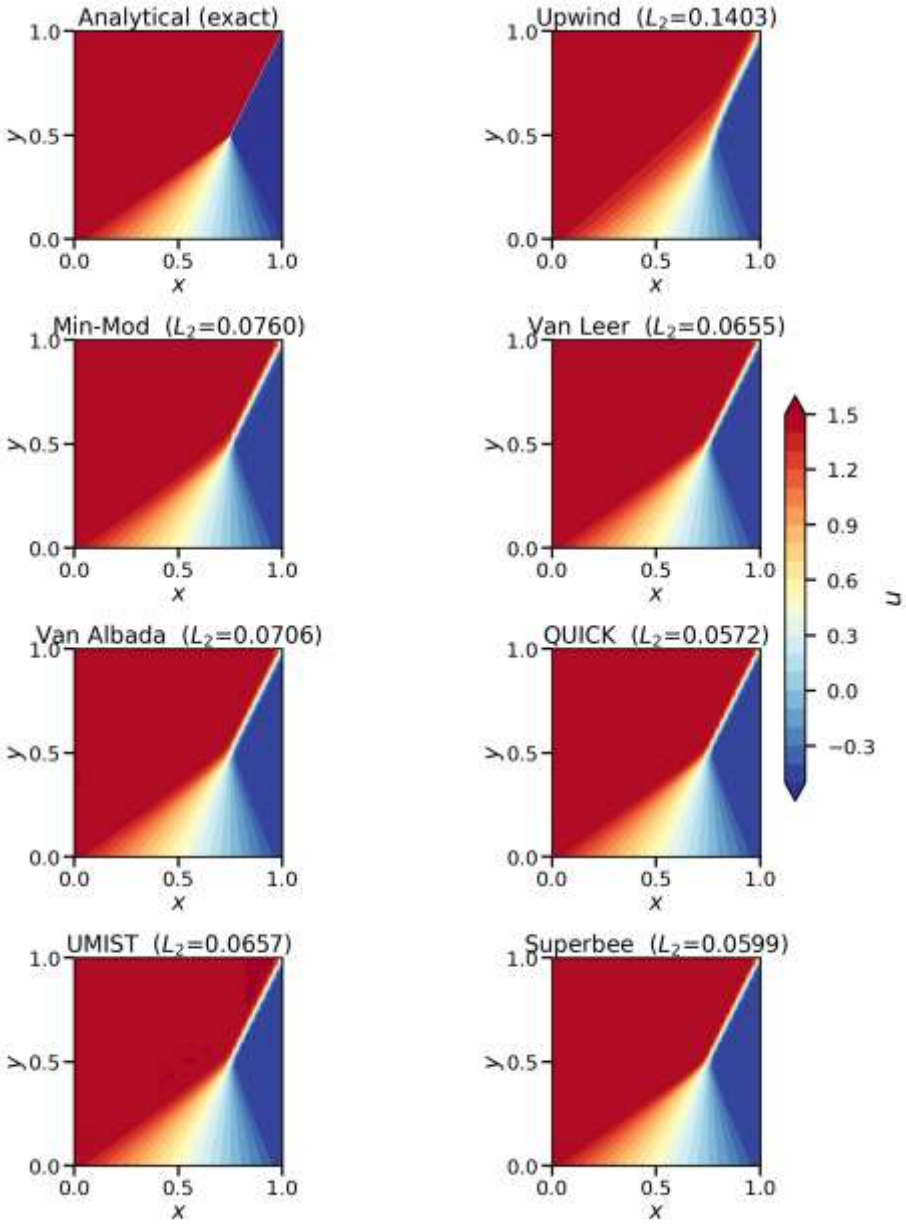


Figure 11 Comprehensive comparison of all flux limiters at N = 41

Table 4 Quantitative comparison of the upwind scheme and the TVD limiters at N = 41 (Case 1). Shock thickness is the 5–95% width of the transition, in cells; TV is the total variation along the same probe lines, whose exact value is |c − d| = 2.0000; the last column is the largest CFL number at which the residual reached 10^{-6}.

Scheme	L1 error	L2 error	L1 reduction (%)	Shock thickness (cells)	TV	CFL
Upwind	0.04117	0.14032	–	3.86	2.0000	0.50
Min-Mod	0.01649	0.07595	59.9	1.91	2.0000	0.50
Van Albada	0.01566	0.07057	62.0	1.85	2.0000	0.50
Van Leer	0.01451	0.06549	64.8	1.81	2.0000	0.50
UMIST	0.01436	0.06571	65.1	1.81	2.0000	0.50
QUICK	0.01353	0.05720	67.1	1.78	2.0000	0.25
Superbee	0.01374	0.05991	66.6	1.73	2.0000	0.10

Table 4 replaces the qualitative ranking of the earlier version with measured quantities. Three of them are worth singling out. First, shock thickness: the first-order upwind scheme spreads the discontinuity over 3.86 cells, whereas every TVD limiter roughly halves this, the sharpest being Superbee at 1.73 cells. Second, accuracy: relative to the upwind scheme the limiters reduce the L1 error by between 60% and 67%, with QUICK giving the lowest L2 error (0.05720 against 0.14032 for upwind). Third, monotonicity: the total variation measured along the probe lines is 2.0000 for every scheme, exactly equal to the imposed jump |c − d|, which confirms numerically that none of the limiters produces an overshoot and that the discrete operator is monotonicity-preserving in the sense of the TVD constraint.

These gains are not free, and the cost appears as a penalty in convergence rather than in accuracy. Most of the limiters drive the residual below 10^{-6} at the same CFL number of 0.5 used for the upwind scheme and in a comparable number of iterations; Van Leer, for example, converges in 224 iterations against 179 for the upwind scheme. The most compressive limiters do not. With QUICK at CFL 0.5 the residual stops falling at about 3×10^{-2} and simply oscillates there: over the last 200 of 1500 iterations it varies between 2.8×10^{-2} and 3.9×10^{-2}. This is the signature of a limit cycle, in which the limiter switches on and off from one iteration to the next in the cells adjacent to the shock, so that no steady state is ever reached. Halving the CFL number to 0.25 removes the cycle and the residual then falls below 10^{-6} in 335 iterations. Superbee behaves in the same way but at a much smaller amplitude: at CFL 0.5 its residual settles between 2.6×10^{-4} and 2.8×10^{-4} and stops improving, and the CFL number had to be reduced to 0.10

before the tolerance was met, which then took 1170 iterations. The amplitude of the plateau falls with the time step — for Superbee from 2.7×10^{-4} at CFL 0.5 to 5.4×10^{-6} at CFL 0.25 — which is consistent with the residual floor being set by limiter switching over one time step rather than by an error in the discretisation. The practical consequence is that the sharpest limiters are the least convenient to drive to a steady state, and their advantage in shock resolution is partly offset by the extra effort needed to converge them.

This also corrects a result reported in the earlier version of this paper. The QUICK limiter was previously found to be markedly less accurate than the other limiters, which is what a computation stopped in the limit cycle would show. Once the CFL number is reduced so that the residual actually converges, QUICK is among the most accurate of the limiters tested. The oscillatory pattern previously visible in the QUICK panel of the limiter comparison was thus a signature of an unconverged steady state rather than a property of the limiter, and it is absent once the residual has converged.

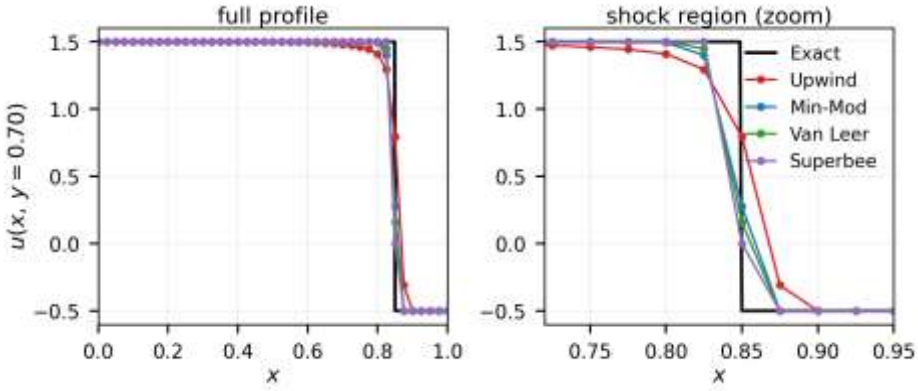


Figure 12 Solution profiles across the shock at y = 0.70 for N = 41, showing the shock thickness of each scheme against the exact solution.

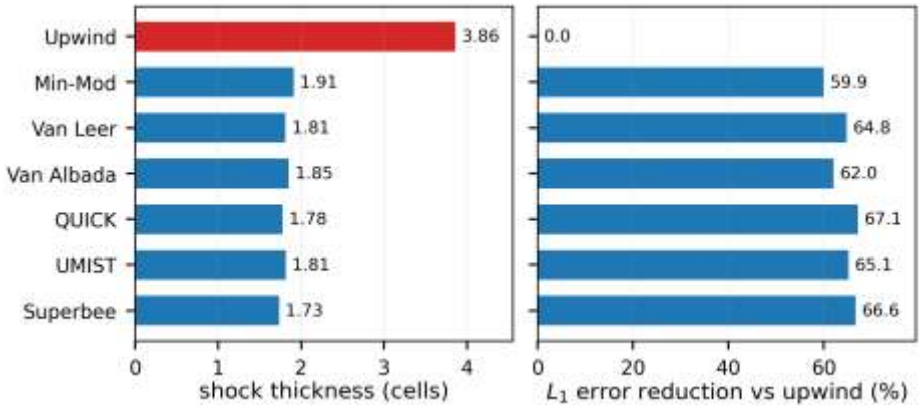


Figure 13 Measured shock thickness in cells (left) and L1 error reduction relative to the first-order upwind scheme (right) for each limiter at N = 41.

From the error comparison plots, increasing the grid from N=21 to N=41 consistently reduces the error across limiters, with the largest gains appearing near the shock front. The comprehensive comparison highlights that the dominant differences occur along the discontinuity, while the smooth regions remain similar across schemes.

4.4 Comparison per Cases

The theoretical shock angle (measured from the vertical y-axis) can be predicted using the ratio of characteristic speeds:

$$\frac{dx}{dy} = \frac{\lambda_{shock}}{\lambda_y} = \frac{a(u_L+u_R)/2}{b} \tag{25}$$

4.4.1.1 Case 1: Reference Case ($\mathbf{a = 1, b = 1}$)

With boundary values $c = 1.5$ and $d = -0.5$, the average shock speed in the x-direction is $S = 1.0\ (1.5 - 0.5)/2 = 0.5$. Since the vertical velocity is $b = 1.0$, the theoretical slope of the shock in the x-y plane is:

$$\frac{dx}{dy} = \frac{0.5}{1.0} = 0.5 \tag{26}$$

The numerical results successfully replicate this behavior, showing a shock that propagates to the right with a slope of 0.5. The shock originates at $y = 0.5$ where the characteristics from the rarefaction fan intersect.

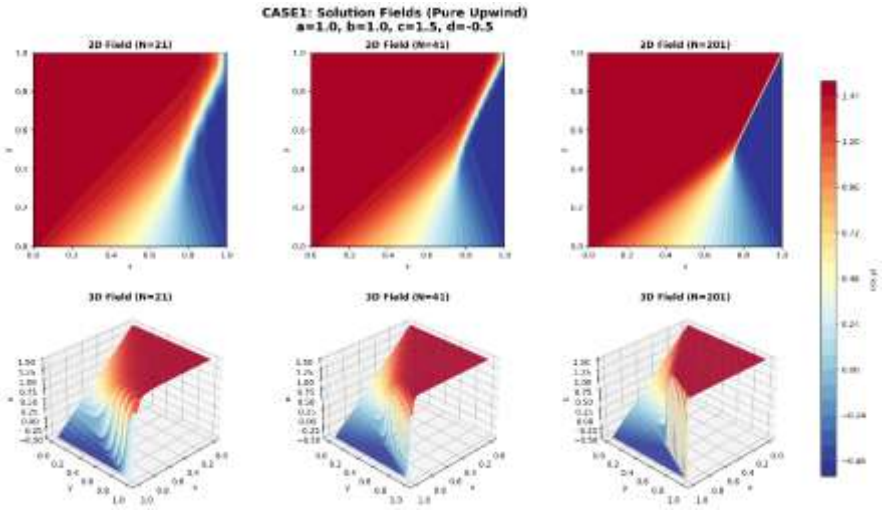


Figure 14 2D and 3D plot for numerical results of each grid sizes for Case 1



Figure 15 Convergence history plot of each grid sizes for Case 1

4.4.2 Case 2: Reduced Vertical Advection ($\mathbf{a = 1, b = 0.5}$)

In Case 2, the vertical advection coefficient b is halved to 0.5 while maintaining the same x-direction parameters as the base case.

- Physical Interpretation: A lower b value signifies that the fluid moves slower in the y-direction relative to the x-direction. Consequently, for every unit of distance traveled vertically, the fluid travels further horizontally.
- Shock Geometry: The theoretical shock slope becomes:

$$\frac{dx}{dy} = \frac{0.5}{0.5} = 1.0 \tag{27}$$

This indicates a much steeper tilt to the right compared to Case 1. The shock will reach the right boundary (x = 1) at a lower y-coordinate than in the reference case.

- Numerical Observation: The simulation results confirm this increased "shearing" effect. The discontinuity is more angled, and the rarefaction fan at the bottom spreads wider in the x-direction before converging into the shock, as the characteristic information travels further horizontally before moving up.

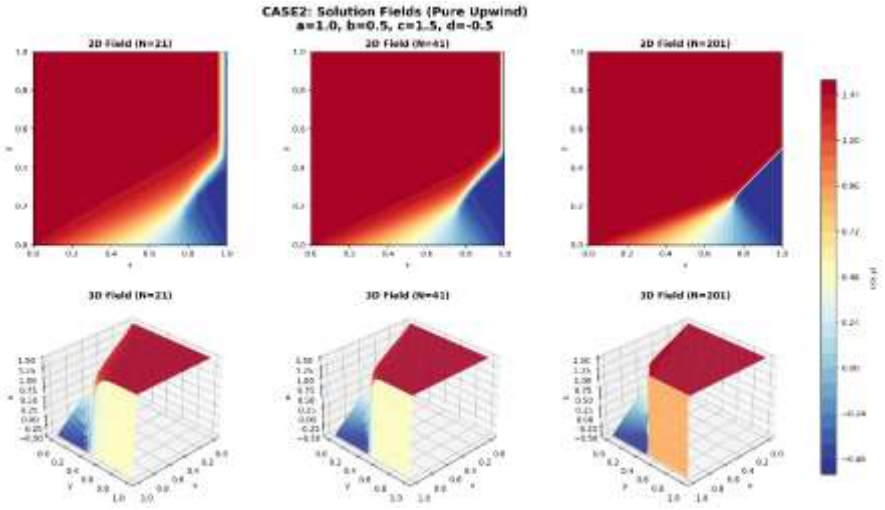


Figure 16 2D and 3D plot for numerical results of each grid sizes for Case 2

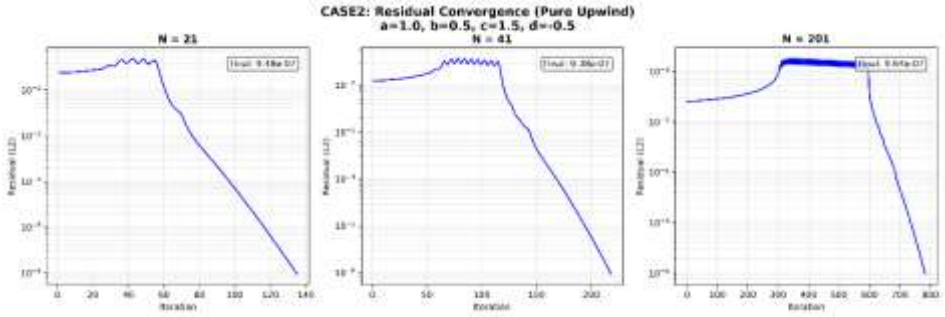


Figure 17 Convergence history plot of each grid sizes for Case 2

4.4.3 Case 3: Increased Nonlinear Convection ($\mathbf{a = 2, b = 1}$)

In Case 3, the nonlinear coefficient a is doubled to 2.0.

- Physical Interpretation: Doubling a increases the nonlinear wave speeds ($\lambda_x = au$) and the flux magnitude in the x-direction. The system becomes more dominated by the nonlinear term $u\frac{\partial u}{\partial x}$.
- Shock Geometry: The average shock speed increases proportionally with a:

$$S = 2.0 \cdot \frac{1.5+(-0.5)}{2} = 1.0 \tag{28}$$

With $b = 1.0$, the slope becomes:

$$\frac{dx}{dy} = \frac{1.0}{1.0} = 1.0 \tag{29}$$

Geometrically, the solution looks identical to Case 2 (slope of 1.0).

- Numerical Stability: Although the geometry matches Case 2, the numerical stability constraints are stricter. The maximum wave speed in the x-direction is now $\lambda_{max} = 2.0 \times 1.5 = 3.0$ (compared to 1.5 in Case 1). To satisfy the CFL condition, the time step Δt must be roughly halved compared to the baseline case.

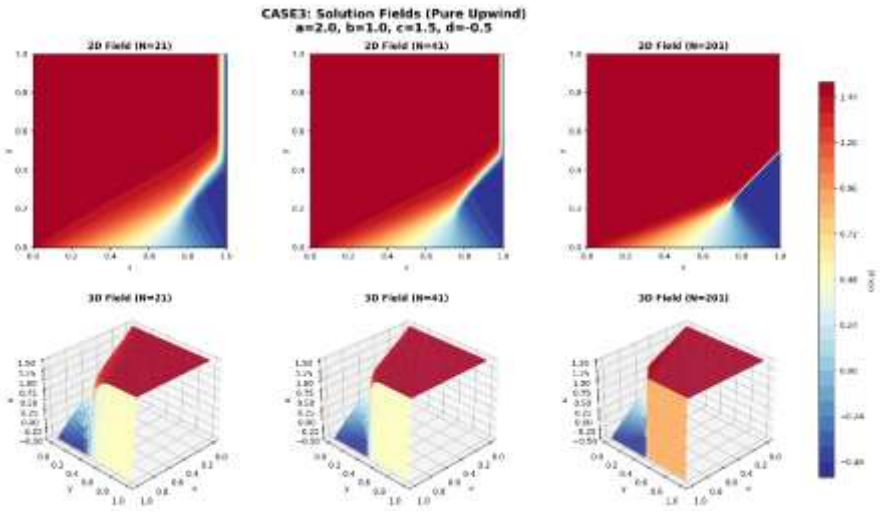


Figure 18 2D and 3D plot for numerical results of each grid sizes for Case 3

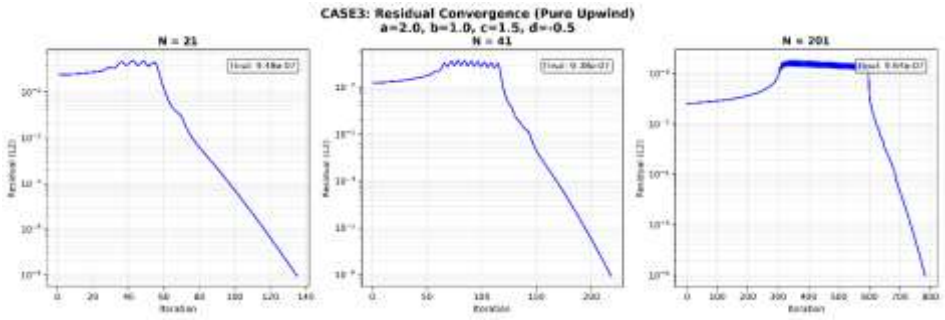


Figure 19 Convergence history plot of each grid sizes for Case 3

4.4.4 Case 4: Weak Shock ($\mathbf{c = 1.0, d = -0.6}$)

Case 4 modifies the boundary values to $c = 1.0$ and $d = -0.6$, while keeping $a = 1, b = 1$.

- Physical Interpretation: The jump across the discontinuity is $\Delta u = 1.0 - (-0.6) = 1.6$, which is smaller than the jump of 2.0 in the other cases.
- Shock Geometry: The average shock speed is significantly reduced:

$$S = 1.0 \cdot \frac{1.0+(-0.6)}{2} = 0.2 \tag{30}$$

With $b = 1.0$, the slope is:

$$\frac{dx}{dy} = 0.2 \tag{31}$$

This produces a very steep shock, propagating almost vertically with a slight drift to the right.

- Numerical Observation: Because the shock moves very slowly to the right, it remains closer to the center of the domain for a longer duration of y. The reduced gradient across the shock (Δu) may result in slightly less numerical diffusion compared to the stronger shocks in Cases $1 - -3$, as the gradient driving the numerical error is smaller.

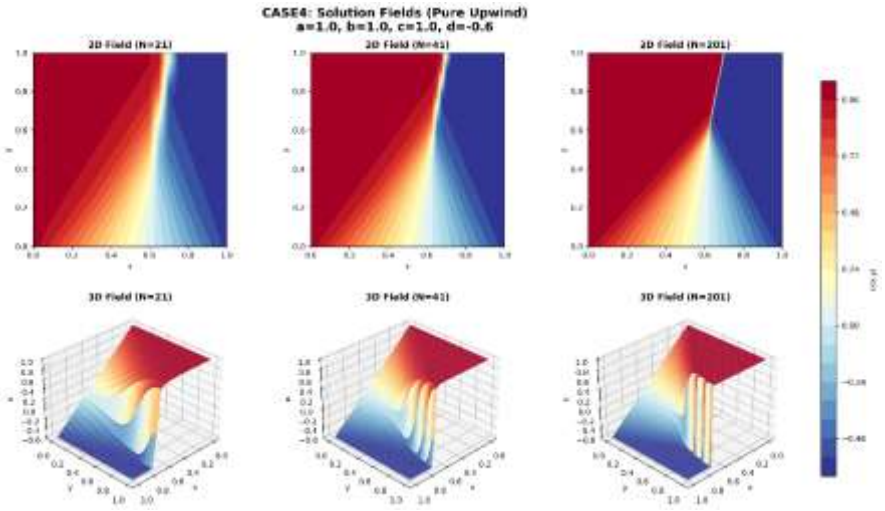


Figure 20 2D and 3D plot for numerical results of each grid sizes for Case 4



Figure 21 Convergence history plot of each grid sizes for Case 4

5 Conclusion

A finite volume solver for the two-dimensional steady inviscid Burgers equation has been implemented and verified against an exact solution obtained by the method of characteristics. Because the steady equation is equivalent to a one-dimensional initial value problem in the time-like coordinate y, the exact solution is available in closed form for every parameter set considered, and it predicts a shock that first appears where the characteristics focus, at $y = 0.5$ for the reference case, and then travels along a straight line at the Rankine–Hugoniot speed. The discrete equations were derived in conservative form, with the nonlinear flux treated in x and the linear flux in y, and the computed shock position and inclination reproduce the analytical prediction in all four cases.

The grid refinement study quantifies the accuracy of the first-order upwind scheme. The observed order of accuracy is 0.86 in the L1 norm, 0.52 in L2 and effectively zero in L∞. This is the expected signature of a monotone first-order scheme applied to a discontinuous solution: the shock is smeared over a fixed number of cells, so the error is O(1) in a layer of width O(h), which integrates to O(h) in L1 and O(√h) in L2 while leaving the maximum error unchanged. The scheme is therefore behaving exactly as theory predicts, and the growth of the L∞ error under refinement reflects the discontinuity rather than any inconsistency in the implementation.

The comparison of limiters can now be stated in measured rather than qualitative terms. At N = 41 the upwind scheme spreads the shock over 3.86 cells; every TVD limiter reduces this to between 1.73 and 1.91 cells and lowers the L1 error by 60 to 67 per cent, while the total variation remains exactly equal to the imposed jump, so monotonicity is preserved throughout. The differences between the limiters themselves are much smaller than the difference between any of them and the first-order scheme. The clearest practical distinction is not accuracy but robustness: the most compressive limiters do not reach steady state at CFL 0.5 and require the time step to be halved, and a limiter stopped in that limit cycle can appear far less accurate than it really is. For problems requiring sharp shock resolution a TVD scheme should be preferred to first-order upwinding, with Van Leer offering the best compromise between resolution and unconditional convergence at the nominal CFL number; the first-order scheme remains appropriate where robustness matters more than resolution.

Several extensions follow naturally from this work. The most immediate is to replace the explicit Euler update with a higher-order strong-stability-preserving Runge–Kutta integrator, which would remove the first-order temporal error and allow the limit cycle affecting the compressive limiters to be examined independently of the time discretisation. A second extension is to the doubly nonlinear form of the two-dimensional Burgers equation, and subsequently to the Euler equations, where the scalar limiters used here must be applied to a characteristic decomposition rather than to a single variable. Finally, the verification methodology used here, an exact solution combined with a measured order of accuracy, could be extended to unstructured or locally refined meshes, for which the interaction between limiter and grid topology is known to be considerably more delicate.

Nomenclature

L_1 = L1 error (mean absolute error)
L_2 = L2 error (root-mean-square error)
L_∞ = L-infinity error (maximum absolute error)
A = Area
E = Nonlinear flux in x-direction, $E(u)$
F = Linear flux in y-direction, $F(u)$
N = Number of grid points in each direction
S = Shock speed
U = Conserved variable
a = Nonlinear convection coefficient (x-direction)
b = Linear advection coefficient (y-direction)
c = Left boundary value
d = Right boundary value
r = Gradient ratio in TVD limiter
u = Solution variable
x, y = Spatial coordinates
Δt = Time step
$\Delta x, \Delta y$ = Grid spacing
λ_x = Characteristic speed in x-direction
λ_y = Characteristic speed in y-direction
ϕ = Face value (numerical flux evaluation)
Ω = Computational domain

TV = Total variation of the discrete solution
h = Grid spacing, h = 1/(N − 1)
k = Ratio of convection coefficients, k = a/b
p = Observed order of accuracy
y_b = Height at which the characteristics focus and the shock forms
x_f = Abscissa of the focusing point
CFL = Courant–Friedrichs–Lewy number

References

[1] Chung, T.J., *Computational Fluid Dynamics,* 2nd ed., Cambridge University Press, 2010.

[2] Burgers, J.M., *A Mathematical Model Illustrating the Theory of Turbulence*, Advances in Applied Mechanics, **1**, pp. 171-199, 1948.

[3] Sharma, A., & J. K.C, Durga., *Burgers' Equation and Traffic Flow*, Journal of the Institute of Engineering, **17**(1), pp. 1-7, 2023.

4] LeVeque, R.J., *Finite Volume Methods for Hyperbolic Problems*. Cambridge, U.K.: Cambridge University Press, 2022.

[5] Toro, E.F., *Riemann Solvers and Numerical Methods for Fluid Dynamics: A Practical Introduction*, 3rd ed., Springer, 2009.

[6] Moelyadi, M.A., *Slide Kuliah: Computational Fluid Dynamics II*, Bandung Institute of Technology, 2023.

[7] Godunov, S.K., *A Difference Method for Numerical Calculation of Discontinuous Solutions of the Equations of Hydrodynamics*, Matematicheskii Sbornik. Novaya Seriya, **47**(89): 3, pp. 271-306, 1959.

[8] Harten, A., *High Resolution Schemes for Hyperbolic Conservation Laws,* Journal of Computational Physics, **49**(3), pp. 357-393, 1983.

[9] Sweby, P.K., *High Resolution Schemes Using Flux Limiters for Hyperbolic Conservation Laws*, SIAM Journal on Numerical Analysis, **21**(5), pp. 995-1011, 1984.

[10] Leer, B.V., *Towards the Ultimate Conservative Difference Scheme. II. Monotonicity and Conservation Combined in a Second-Order Scheme,* Journal of Computational Physics, **14**(4), pp. 361-370, 1974.

[11] Albada, G.D.B., Leer, B.V., & Roberts, W.W.Jr., *A Comparative Study of Computational Methods in Cosmic Gas Dynamics,* Astronomy and Astrophysics, **108**(1), pp. 76-84, 1982.

[12] Leonard, B.P., *A Stable and Accurate Convective Modelling Procedure Based on Quadratic Upstream Interpolation,* Computer Methods in Applied Mechanics and Engineering, **19**(1), pp. 59-98, 1979.

[13] Lien, F.S., & Leschziner, M.A., *Upstream Monotonic Interpolation for Scalar Transport With Application to Complex Turbulent Flows*, International Journal for Numerical Methods in Fluids, **19**(6), pp. 527-548, 1994.

[14] Courant, R., Friedrichs, K., & Lewy, H., *Uber Die Partiellen Differenzengleichungen Der Mathematischen Physik*, Mathematische Annalen, **100**(1), pp. 32-74, 1928.
[15] Whitham, G.B., *Linear and Nonlinear Waves,* Wiley-Interscience, 1974.
[16] Lax, P.D., *Hyperbolic Systems of Conservation Laws II*, Commun. Pure and Applied Mathematics, **10**(4), pp. 537–566, 1957.
[17] Evans, L.C., *Partial Differential Equations*, 2nd ed., American Mathematical Society, 2010.
[18] Roache, P.J., *Code Verification by the Method of Manufactured Solutions,* Journal Fluids Engineering, **124**(1), pp. 4–10, 2002.
[19] Roy, C.J., *Grid Convergence Error Analysis for Mixed-Order Numerical Schemes,* AIAA Journal, **41**(4), pp. 595–604, 2003.

Appendix. Exact Solution by the Method of Characteristics

At steady state the governing equation divided by b reads $\partial u/\partial y + k \cdot u \cdot \partial u/\partial x = 0$ with $k = a/b$, an initial value problem in the time-like coordinate y whose data are supplied by the bottom boundary, $u(x, 0) = c - (c - d)x$. The solution is constant along a characteristic, so the characteristics are the straight lines [15], [17]

$$x(y) = x_0 + k \cdot u_0(x_0) \cdot y, \quad u_0(x_0) = c - (c - d)x_0 \quad \text{(A1)}$$

Neighbouring characteristics intersect where $\partial x/\partial x_0 = 1 - k(c - d)y$ vanishes. Since this derivative does not depend on x_0, every characteristic leaving the interval $0 \le x_0 \le 1$ focuses at the same height,

$$y_b = b / [a(c - d)] \quad \text{(A2)}$$

and at that height they all pass through the single abscissa

$$x_f = c / (c - d) \quad \text{(A3)}$$

For the reference case ($a = b = 1$, $c = 1.5$, $d = -0.5$) this gives $y_b = 0.5$ and $x_f = 0.75$. This is the origin of the shock quoted in Section 4, and it answers the question of why the discontinuity first appears at $y = 0.5$: that height is not imposed on the problem but is the level at which the compressive part of the bottom profile first becomes multivalued. Below y_b the map $x_0 \to x$ is invertible, and inverting it gives the compression fan bounded by the extreme characteristics $x = k \cdot c \cdot y$ and $x = 1 + k \cdot d \cdot y$, outside which u keeps its boundary values c and d.

Above y_b the solution is completed by a single shock whose inclination follows from the Rankine–Hugoniot condition applied to the flux pair (E, F) [4], [5], [16],

$$dx_s/dy = [E(u_L) - E(u_R)] / [F(u_L) - F(u_R)] = a(u_L + u_R) / (2b) \quad \text{(A4)}$$

With $u_L = c$ and $u_R = d$ the shock is the straight line $x_s(y) = x_f + [a(c + d)/(2b)] \cdot (y - y_b)$, and it is admissible because the Lax entropy condition $a \cdot u_L > b \cdot dx_s/dy > a \cdot u_R$ is satisfied [16]. For Case 1 this is $x_s = 0.5 + 0.5y$, so the shock starts at (0.75, 0.5) and leaves the domain exactly at the corner (1, 1). Evaluating the construction for Case 1 gives the piecewise solution below, which was verified against the general expression to machine precision (maximum difference 3.8×10^{-15}).

Lower Domain ($y < 0.5$)

In the lower region, the solution exhibits a compression fan followed by two constant states:

$$u(x,y) = f(x) = \begin{cases} 1.5, & if\ x < 1.5y \\ \frac{1.5-2x}{1-2y}, & if\ 1.5y \le x \le (1-0.5y) \\ -0.5, & if\ x \ge (1-0.5y) \end{cases} \quad \text{(A5)}$$

Upper Domain ($y \geq 0.5$)

In the upper region, a shock wave forms due to the intersection of characteristics:

$$u(x,y) = f(x) = \begin{cases} 1.5, & if\ x \le 0.5 + 0.5y \\ -0.5, & if\ x > 0.5 + 0.5y \end{cases} \quad \text{(A6)}$$

The shock forms at $(x, y) = (0.75, 0.5)$ and propagates with a slope of 0.5.

The construction above holds for arbitrary a, b, c and d, so an exact solution exists for every case in Table 1; the corresponding parameters are collected in Table 5. Because the steady solution depends on a and b only through k = a/b, Cases 2 and 3 share the same exact solution, which is why their computed fields and error norms in Section 4.4 agree to five significant figures despite having different coefficients. The final column reports the height at which the shock crosses the right boundary; where this is less than one the shock leaves the domain and the Dirichlet condition on that boundary is no longer compatible with the characteristics, which is the reason Case 1 is used as the reference for quantitative verification.

Table 5 Shock parameters of the exact solution for the four cases, with the error norms of the upwind solution at N = 201.

Case	k = a/b	Breaking height	Focus abscissa	Shock slope	Shock exits at	L2 error
Case 1	1.0	0.500	0.750	0.50	1.00	0.06020
Case 2	2.0	0.250	0.750	1.00	0.50	0.11422
Case 3	2.0	0.250	0.750	1.00	0.50	0.11422
Case 4	1.0	0.625	0.625	0.20	outside	0.03216

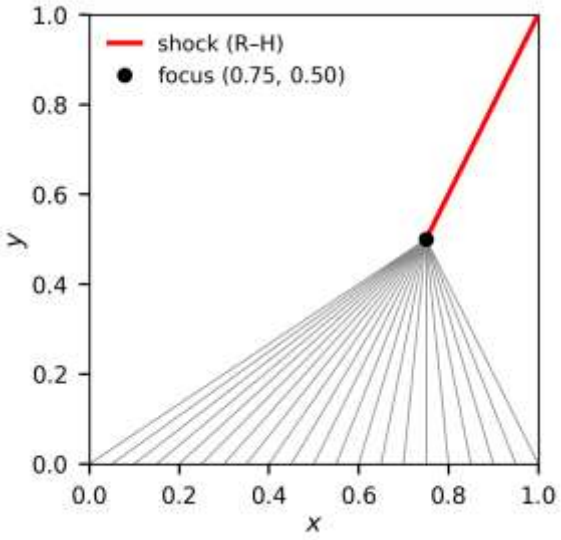


Figure 22 Characteristics of the reference case focusing at (0.75, 0.5) and the resulting Rankine–Hugoniot shock path.